Correlative light and electron microscopy : strategies and applications

Driel, L.F. van

Citation

Driel, L. F. van. (2011, October 11). *Correlative light and electron microscopy : strategies and applications*. Retrieved from https://hdl.handle.net/1887/17922

Chapter 2

Fluorescent Labeling of Resin-Embedded Sections for Correlative Electron Microscopy Using Tomography-Based Contrast Enhancement

Linda F. van Driel, Kèvin Knoops, Abraham J. Koster, Jack A. Valentijn.

Department of Molecular Cell Biology, Section Electron Microscopy, Leiden University Medical Center, Leiden, The Netherlands

Journal of Structural Biology
161(3):372-83. 2007.

Abstract

Locating areas of interest by electron microscopy can be laborious. This is particularly true for electron tomography, where the use of thicker sections may obscure relevant details in the projection images. We evaluated the applicability of fluorescent probes to thin plastic sections, in combination with fluorescence microscopy, as an aid in selecting areas for subsequent electron microscopic analysis. We show that pre-embedding labeling of DNA and RNA with acridine orange yielded a predominant nuclear stain. The stain greatly reduced the time needed to scan sections for mitotic cells, or cells with characteristic nuclei such as neutrophils. Post-embedding labeling with SYTOX green yielded a nuclear stain comparable to acridine orange, and Wheat Germ Agglutinin (WGA) conjugated to Alexa Fluor 488 labeled mucous granules and the Golgi area in intestinal goblet cells. The fluorescent labels were visualized directly on sections on electron microscope grids. It was therefore possible to establish a coordinate system based on the position of the grid bars, allowing for easy retrieval of selected areas. Because the fluorescent probes were incompatible with osmium tetroxide treatment, contrast in the sections was faint. We propose a simplified electron tomography procedure for the generation of 2D views with enhanced contrast and resolution.

Introduction

Correlative light and electron microscopy (CLEM) encompasses all microscopic techniques that aim at imaging the same area in a specimen by using photons and electrons sequentially as the image-forming sources. The combination of these two imaging modalities offers specific advantages. Thus the relatively low-magnification range of light microscopy (LM) is ideal for locating areas of interest for subsequent high-resolution imaging by transmission electron microscopy (TEM). For comparison, typical fields of view are 50 by 50 µm with a resolution of 200 nm for LM, and 4 by 4 µm with a resolution of 1 nm for TEM. Performing the search for areas of interest directly by TEM can be as laborious as finding the proverbial needle in a haystack due to the higher magnification range at which TEM operates (Koster and Klumperman, 2003). This is particularly true for electron tomography, where the use of thicker sections may obscure relevant details in 2D search mode due to the superimposing of 3D structural information in the 2D projection image. For cryoelectron microscopy the challenge to locate an area of interest is even greater, since the low-dose requirements prohibit extensive searching, and the low contrast provides little visible morphological information in the 2D image (Braet et al., 2007; McIntosh et al., 2005; Steven and Aebi, 2003). An additional important advantage of LM is that it allows for the imaging of dynamic processes in live cells, thereby establishing a history of the cells and, as a consequence, adding considerably to the interpretational gain of subsequent ultrastructural analyses by TEM or electron tomography (Svitkina and Borisy, 1998).

Although CLEM techniques have been available and applied in many research projects within the life sciences for several decades, they have not yet become mainstream tools despite the obvious benefits outlined above. One reason for CLEM remaining on the fringe of TEM and electron tomography applications is that the currently available protocols often appear highly specialized and therefore suitable only for addressing a limited number of questions. Another reason is that many of the existing procedures seem arduous, cumbersome, and requiring special skills. Several factors contribute to these current drawbacks. First of all, there is no golden standard yet for an intermodal coordinate system that permits easy retrieval at the TEM level of an area of interest preselected by LM. Moreover, the transition from LM to TEM often involves additional processing such as embedding and ultrathin sectioning, which can lead to changes in orientation of the sample (Biel et al., 2003; Giepmans et al., 2005; Mironov et al., 2000). Secondly, there are considerable differences between LM and TEM with respect to the preparation of biological samples, and their unification often implies a compromise between stainability and ultrastructural preservation (Giepmans et al., 2006). For instance, osmium tetroxide, a commonly used postfixative that generates contrast for TEM on plastic-embedded material, is incompatible with most LM staining or labeling procedures. Thirdly, different detection systems are employed to localize specific molecules by LM or by TEM (Giepmans et al., 2006; Grabenbauer et al., 2005). Although progress is being made in the development of multimodal probes (Corstjens et al., 2005; Deerinck et al., 2007; Giepmans et al., 2005; Najlah and D'Emanuele, 2006; Powell et al., 1998;

Takizawa and Robinson, 2000), there are no routine methods yet for the correlated localization of biomolecules.

It is, however, common practice in most electron microscopy laboratories to cut semi-thin (0.3-0.5 µm) plastic sections adjacent to ultra-thin (50-70 nm) sections; the semi-thin sections are stained with toluidine blue to provide contrast for light microscopic examination (McNary et al., 1964). This procedure is very useful to provide a general overview of the sample area as a prelude to the electron microscopic investigation of the ultra-thin sections. However, due to the considerable thickness of the semi-thin sections, it is not possible to browse for fine details such as subcellular structures, or even whole cells, as they may not be present anymore in the adjacent ultra-thin sections. The ultra-thin sections cannot be stained directly since they absorb too little toluidine blue (or similar chromophores) to generate sufficient contrast (Jones et al., 1982). Much weaker signals can be detected when fluorescent stains are used instead of chromophores (McNary et al., 1964). Biel et al. developed a method for the fluorescent staining of resin-embedded skin tissue by adding fluorescent dyes, such as acridine orange and safranin O, to the substitution medium during freeze-substitution (Biel et al., 2003; Pfeiffer et al., 2003). The fluorescent signals are then recorded by imaging in the specimen block using 3D confocal laser scanning microscopy, and subsequent electron micrographs acquired from ultrathin sections are matched with an optical slice from the 3D volume (Biel et al., 2003).

The present paper reports our efforts to develop more universally applicable protocols for CLEM. We focused on feasible procedures that allow for the fluorescent staining of thin sections of resin-embedded cells and tissues. These stains provide landmarks to facilitate the browsing of complex tissues, and also enable the detection of rarely occurring features that would otherwise be extremely difficult to find. Finally, we propose the use of electron tomography with a minimum number of tilt angles to generate 2D images with improved contrast and satisfactory ultrastructural detail despite the lack of osmification.

Materials and Methods

Sample preparation

Vero-E6 cells and mouse fibroblast (3T3) cells were grown on Thermanox in DMEM supplemented with 8% fetal calf serum and antibiotics under standard cell culture conditions. Cells were cryo-immobilized in a custom-built plunge-freezing apparatus by blotting them for one second in a humidity- and temperature-controlled chamber, followed by plunging in liquid ethane. The frozen-hydrated cells were transferred into vials containing a frozen solution of 0.5% uranyl acetate in anhydrous acetone. The samples were then freeze-substituted using an automated freeze substitution apparatus (AFS System, Leica, Wetzlar, Germany). Following freeze substitution, the cells were flat embedded in lowicryl HM20 (Agar scientific ltd., Essex, United Kingdom), which was polymerized for 72 hours under UV light.

Adult male Wistar rats (Harlan, Horst, the Netherlands) were used as donors of duodenum and pancreas tissue. The animals were sacrificed by cervical dislocation. The duodenum was quickly removed, rinsed in phosphate-buffered saline (PBS), cut in pieces of about 1mm3, and fixed in 4% paraformaldehyde. The tissue fragments were subsequently embedded in lowicryl HM20 at -30˚C by means of progressive lowering of temperature (PLT). This method has been shown to provide good ultrastructural and antigenic preservation (Robertson et al., 1992). Pancreas tissue was further dissected to obtain lobules of exocrine tissue, as previously described (Amsterdam et al., 1978; Valentijn et al., 1999), and subsequently high-pressure frozen in an EMPACT-2 apparatus (Leica). Following high-pressure freezing, the samples were transferred to the AFS system, freeze-substituted as described above, and embedded in lowicryl HM20.

Tissue of an abdominal aortic aneurysm was removed from a patient during surgery. A skeletal muscle biopsy was obtained from a presymptomatic carrier of oculopharyngeal muscular dystrophy. The tissues were collected in a physiological salt solution at 4 °C. In the laboratory, the tissues were immediately cut into pieces of about 1 mm3, fixed overnight in 4% paraformaldehyde, and embedded in HM20 using the PLT procedure.

Resin embedded cell and tissue blocks were trimmed, and sections of 70-150 nm were cut on a Leica ultramicrotome UC6. Sections were collected on 75 Mesh copper grids coated with formvar and carbon.

Fluorescent staining and fluorescence microscopy

Vero cells, muscle tissue, and aneurysm tissue were fluorescently labeled by including 0.1% acridine orange in the freeze substitution medium. Post-embedding labeling was carried out directly on the EM-grids carrying thin sections of resin-embedded rat duodenal or pancreatic tissue. The sections were labeled with the fluorescent dyes SYTOX green (1 µM; Invitrogen, Breda, the Netherlands) in H2O (20 minutes at room temperature), or Alexa Fluor 488-conjugated Wheat Germ Agglutinin (0.01%; Invitrogen) in PBS (30 minutes at room temperature). The grids were subsequently washed three times with H2O, air dried, and dry-mounted on a glass slide with cover slip. Other sections were labeled with antibodies for fluorescent detection. For this purpose, the sections were incubated with blocking buffer (PBS containing 1% BSA and 5% fetal calf serum) for 30 min, followed by primary antibodies diluted in blocking buffer for one hour at 37˚C. Primary antibodies tested were mouse anti-β-tubulin (diluted 1:200; Sigma, Missouri, USA), rabbit anti-ZO-1 (diluted 1:50; Zymed Laboratories, Carlsbad, USA), and mouse anti-actin and rabbit anti-laminin (both diluted 1:50; Abcam, Cambridge, UK). Sections were subsequently washed four times one minute with blocking buffer, followed by secondary antibody incubation for one hour with either goat anti mouse IgG alexa fluor 488, or goat anti rabbit IgG alexa fluor 568 (both diluted 1:200; Molecular Probes/Invitrogen, Eugene, USA/Paisley, United Kingdom).

Thereafter, the sections were washed four times in PBS and five times in H2O. We also tested the mouse monoclonal antibodies with an amplification kit using both secondary and tertiary Alexa Fluor 488-conjugated antibodies, according to the manufacturer's protocol (Molecular Probes/Invitrogen). In a number of experiments, sections were etched with a saturated solution of NaOH in absolute ethanol (2-3 s) prior to the immunocytochemistry.

Fluorescently stained thin sections of cells and tissues were examined either with a Leica SP2 confocal microscope, or with a Leica DMRB fluorescence microscope equipped with a Photometrics CH250 CCD camera. Grid scans were made by taking partly overlapping images with a 10x objective (numerical aperture: 0.3), and by stitching of these images using the Photomerge tool in Adobe Photoshop. The grid scans provided overviews used to facilitate the retrieval of areas of interest by subsequent TEM. Images of higher magnification were taken using either a 40x objective with a numerical aperture of 1.00, or a 63x objective with a numerical aperture of 1.32.

RNAse and DNase treatment

Vero E6 cells grown on Thermanox were fixed with 3% PFA for 1h and permeabilized using 0.1% TX-100 in PBS (10 min). RNase treatment was performed with 1 mg/ml RNaseA (Qiagen, Venlo, the Netherlands) in PBS for 15 min at RT whereas for the DNase treatment, the cells were incubated with 100 U/ml DNase (Invitrogen) in PBS for 1h at 37 ºC. After intensive washing with PBS, cells were plunge-frozen and further processed for en bloc acridine orange staining as described above.

Transmission electron microscopy and tomography

Regions of interest identified by fluorescence microscopy were retrieved in a CM10 transmission electron microscope (Phillips, Eindhoven, the Netherlands) for ultrastructural examination. The microscope was operated at an accelerating voltage of 80 kV, and digital electron micrographs were acquired with a MegaView III CCD camera (SIS GmbH, Herzogenrath, Germany). electron tomography was carried out using a Tecnai 12 transmission electron microscope (FEI Company, Eindhoven, the Netherlands) at 120 kV, equipped with a 4k Eagle CCD camera (FEI Company). Colloidal gold particles of 10 nm were attached to the formvar side of the grid, and used as fiducial markers. Tilt series from +65° to -65° were collected with 1° increments using XPlore3D software (FEI Company). 3D reconstructions were generated using the IMOD software package (Kremer et al., 1996).

Results and Discussion

In the vast array of possible strategies for CLEM, we opted for the fluorescent staining of ultrathin plastic sections because of their widespread use in cell biology, ultrastructural pathology, and electron tomography. Furthermore, others and us have recently developed an integrated system for CLEM comprising a laser scanning fluorescence microscope built into a commercially available transmission electron microscope. This system, which will be described elsewhere (AV Agronskaia, JA Valentijn, LF van Driel, CTWM Schneijdenberg, BM Humbel, P van Bergen en Henegouwen, AJ Verkeij, AJ Koster, and HC Gerritsen, manuscript in preparation), requires CLEM labeling techniques of the kind proposed herein, where a fluorescent signal can be detected directly on ultrathin plastic sections.

We first set about determining whether the pre-embedding fluorescent staining of specimen blocks, developed by Biel et al. (2003; see Introduction), could also be employed to detect the fluorescence directly in ultrathin sections, as this would greatly facilitate, and at the same time improve, the correlation between LM and TEM. Vero cells, a skeletal muscle biopsy, and surgically removed abdominal aneurysm tissue were embedded in either lowicryl HM20 or Epon, following freeze-substitution (Vero cells) or progressive lowering of temperature (muscle and aneurysm). Acridine orange was added to the substitution medium. This dye emits green fluorescence when bound to double stranded DNA and red fluorescence when bound to RNA or single stranded DNA (Rigler, 1966). Ultra-thin (70 nm) and thin (100-150 nm) sections were collected on TEM grids and subsequently sandwiched between a microscope slide and coverslip. In all three samples, acridine orange staining was easily detected in both ultra-thin and thin sections. Fig. 1 illustrates the staining pattern we observed in the skeletal muscle tissue. In this example, acridine orange stained the nuclei at the periphery of individual muscle fibers. The overview in Fig. 1A shows the area of an EM grid that contained 3 serial sections. The overview was generated by merging of 8 partly overlapping fluorescence micrographs acquired at low magnification (20X objective). Because the bars of the copper TEM grids stood out in the fluorescence micrographs (see below), the merging of the images could be performed in a straightforward manner using the automated photomerge tool in Adobe Photoshop (Adobe Systems Inc., San Jose, CA). The merged images were used as maps via which areas of interest could be retrieved by TEM. For this, the presence of the grids' bar pattern was also very helpful. Depending on the complexity of the specimen, it took one to several minutes to retrieve an area of interest. Fig. 1B displays an enlargement of a grid quadrant with cross-sectioned muscle fibers outlined by acridine-orange stained nuclei. When compared with a fluorescence micrograph taken when the tissue was still in the specimen block, as shown in Fig. 1C, the signal intensity was appreciably weaker. However, this was not an obstacle for the consistent detection of acridine orange staining. The skeletal muscle tissue was derived from a biopsy of a presymptomatic carrier of oculopharyngeal muscular dystrophy, a disease that is characterized histologically and ultrastructurally by the presence of rimmed vacuoles within muscle fibers, and by inclusions of the

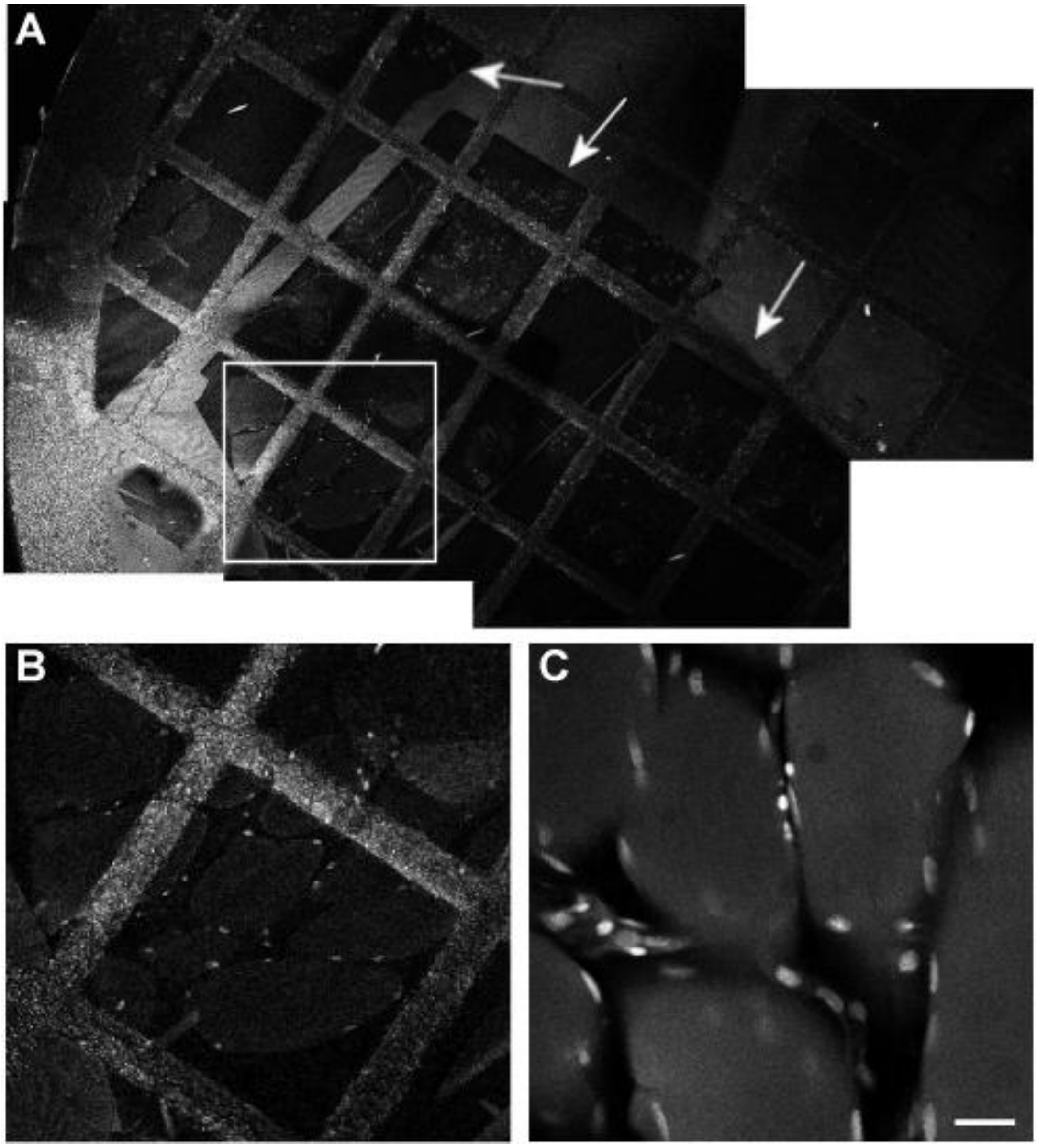

Figure 1: Pre-embedding staining of skeletal muscle tissue with acridine orange. (A) Overview of several 100-nm sections (arrows) of HM20 embedded tissue on a TEM-grid. The image is constructed of eight partly overlapping fluorescent micrographs that were stitched together into one large overview image. Notice the slight autofluorescence of the grid bars. Such an overview with clearly delineated grid bars was used as a tool to orientate in TEM mode. (B) Fluorescence micrograph of a higher magnification of the boxed area in panel A, showing acridine orange labeled nuclei at the periphery of muscle fibers. The circular arrangement of the nuclei indicates that the muscle fibers are cross sectioned. (C) Confocal image taken when the tissue was still in the specimen block. Due to the greater thickness of the optical slice (~500 nm), the fluorescence is more prominent than in the thin section (100 nm) in (B). The grid bars in (A) and (B) are 250 μm apart. Scale bar in (C) represents 10 μm.

nuclei surrounding the muscle fibers (Tome et al., 1997). The intranuclear inclusions have the typical appearance of black holes in nuclei that have been fluorescently labeled for DNA. In the biopsy material we investigated (Fig. 1), there was no evidence of rimmed vacuoles or intranuclear inclusions, consistent with the lack of symptoms of the carrier. The acridine-orange method allowed us to make this observation effortlessly, and had there been an anomaly in the fluorescence pattern, it would have been easy to obtain high-resolution TEM data.

In Vero cells, acridine orange stained not only the nucleus but also the cytoplasm, presumably by binding to RNA (Fig. 2). However, like the nucleus, the cytoplasm was emitting green fluorescence instead of the expected orange fluorescence (compare Fig. 2A with Fig. 2B). The fluorescence in the cytoplasm was considerably weaker than the DNA stain, so that nuclei in interphase cells and chromosomes in mitotic cells were readily detected (Fig. 2B,C). We have currently no explanation for the change in fluorescence emission of acridine orange bound to RNA, but it seems reasonable to suggest that the resin embedding may have altered the interaction of acridine orange with nucleic acids. To exclude the possibility that the green fluorescence in the cells' cytoplasm was due to nonspecific background, we performed control experiments in which fixed Vero cells were treated with either RNase, or DNase, or a cocktail of RNase and DNase, prior to freeze-substitution in the presence of acridine orange. As illustrated by the examples in Fig. 2D, which were all acquired at the same settings for laser intensity, photomultiplier gain and offset, RNase treatment abolished the fluorescence of the cytoplasm and nucleoli, while DNase treatment greatly diminished the nuclear staining. Very little fluorescence was left in the nuclei of cells that were treated with a cocktail of RNase and DNase. Altogether these data indicate that despite the altered fluorescence properties, freeze-substituted acridine orange specifically labels RNA and DNA compartments in resin-embedded specimens.

To further explore the usefulness of acridine orange as a CLEM probe for plastic sections we endeavored to search for a relatively rare cell in a complex tissue. We opted for searching neutrophilic granulocytes in a tissue sample of an abdominal aortic aneurysm. In the connective tissue underneath the lesion, acridine orange yielded an amalgam of staining patterns that reflected the different cell types present, as illustrated in Fig. 3A. The nuclei of lymphocytes stained very bright, whereas those of the abundant fibroblasts were faint but displayed prominent nucleoli. Endothelial cells lining small blood vessels were recognized by their flattened nucleus; the cytoplasm of the endothelial cells was fluorescent as well, but less intense. Neutrophilic granulocytes were detected on the basis of their typically multilobed nucleus, which appeared fragmented in ultrathin sections. Fig. 3B, which is a zoom of Fig. 3A, shows that two cells in the lumen of a blood vessel displayed patches of acridine-orange fluorescence. TEM of cells with a patchy staining pattern confirmed that these cells corresponded to neutrophilic granulocytes, because they displayed a fragmented nucleus and numerous rod-shaped specific granules (Fig. 3C) (Lentz, 1971).

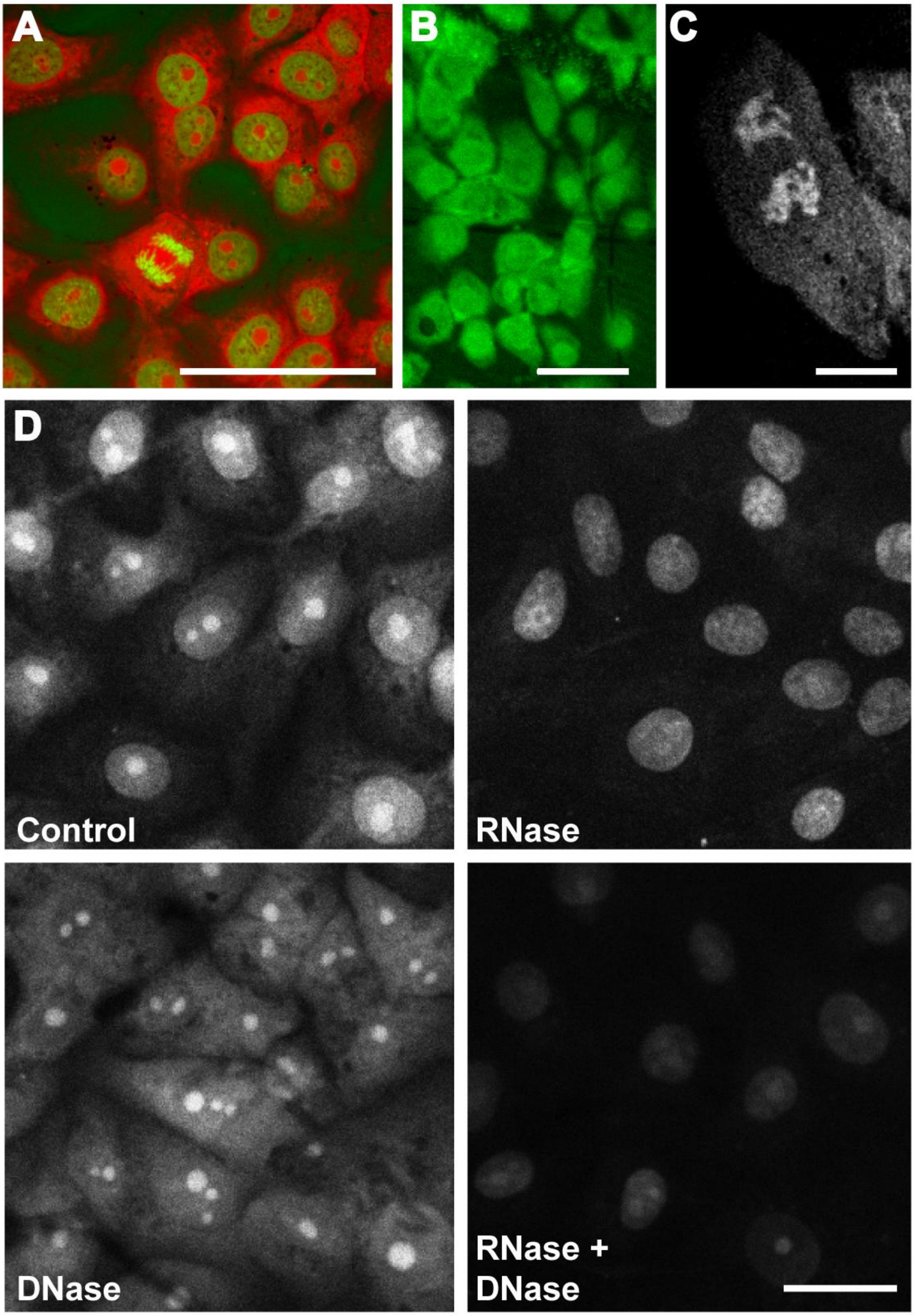

Figure 2: Differences in acridine orange staining before and after HM20 embedding. (A) Chemically fixed Vero cells mounted on a glass slide after acridine orange staining, displaying red fluorescence in the RNA-rich cytoplasm, and green fluorescence in the DNA-rich nuclei. Notice the brightly stained condensed chromosomes in the mitotic cell. (B) HM20 embedded Vero cells in a 100-nm section, stained with acridine orange during freeze substitution. In this condition,

acridine orange emits green fluorescence in both cytoplasm and nuclei. Because the nuclear stain is more intense, the nuclei can still be distinguished. (C) A mitotic Vero cell in another thin section. The condensed DNA results in a bright acridine orange stain. Mitotic cells could thus be located staightforwardly in thin sections. (D) Specificity of the acridine orange stain in resin-embedded cells. After fixation and permeabilization, but prior to freeze-substitution with acridine orange, Vero cells were incubated with either RNase, or DNase, or a mixture of RNase and DNase, as indicated. Control cells underwent the same incubation but without the addition of RNase and DNase. To allow for comparison, images were recorded during the same microscopy session using identical settings for laser intensity, photomultiplier gain and offset. Note that the fluorescence of cytoplasm and nucleoli is absent in the RNase treated cells, while the nuclear stain is greatly reduced in the DNase treated cells. Scale bars: 50 μm in (A), 50 μm in (B), 10 μm in (C), 25 μm in (D).

Taken together, the above data indicate that pre-embedding staining with acridine orange is a straightforward yet powerful method to perform fluorescence microscopy on ultrathin plastic sections, thereby providing a means of orientation in complex specimens and permitting the selection of features of interest for subsequent analysis by TEM. Our next goal was to determine whether thin and ultrathin plastic sections could be stained directly with fluorescent probes. An advantage of using post-embedding fluorescent labeling would be that it offers more flexibility in the choice of probes. We tested a broad spectrum of potential probes on paraformaldehyde-fixed rat duodenal tissue, high-pressure frozen rat pancreatic tissue, and plunge-frozen 3T3 cells. The cells and tissues were embedded in HM20 following PLT (duodenum) or freeze-substitution (pancreas, 3T3 cells). In our hands, immunofluorescence-based detection methods were unsuccessful (Fig. 4). We tested monoclonal antibodies against actin and tubulin, and polyclonal antibodies against laminin and ZO-1 (Zonula Occludens protein 1), in combination with Alexa Fluor 488-conjugated secondary antibodies or protein-A. To give an example, Figure 4A illustrates the lack of appreciable immunofluorescence on a thin section of 3T3 cells immunolabeled with β-tubulin antibodies and detected with Alexa Fluor 488 conjugated protein A. By contrast, when on subsequent sections the fluorescent label was replaced with 15 nm gold particles conjugated to protein A, specific labeling was observed at the TEM level (Fig. 4B). It thus appeared that the antibody signals were too weak to allow for detection by immunofluorescence. We tried to amplify the signal by mild etching of the sections with sodium ethoxide and by an additional incubation step with tertiary antibodies that were also conjugated to Alexa Fluor 488, but these efforts were to no avail. Successful antibody labeling has been reported for semithin and thin epoxy sections using a combination of surface etching with sodium ethoxide and heat-induced antigen retrieval (Cai et al., 2005; Groos et al., 2001), and for ultrathin cryosections (Mori et al., 2006; Takizawa and Robinson, 2003). It is possible that the heat-treated epoxy sections and the cryosections have more antigen-binding sites available for the antibodies, but antibody-specific differences in affinity and diffences in epitope density may also contribute to the discrepancy between the present and previous data.

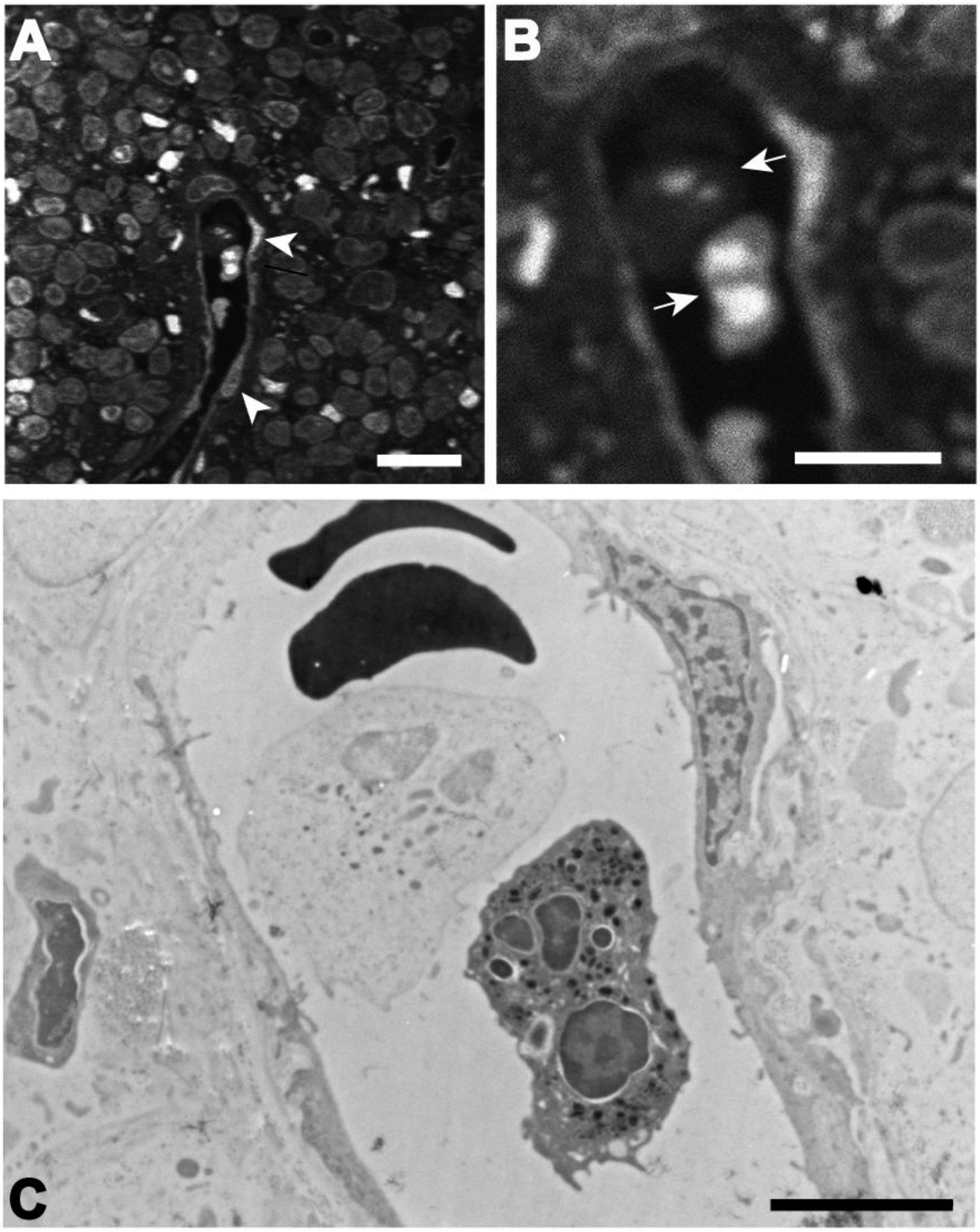

Figure 3: Pre-embedding staining of abdominal aneurysm tissue with acridine orange, visualized in a 100-nm HM20 section on a TEM-grid. (A) Confocal image of a connective tissue area with numerous acridine-orange labeled nuclei. Notice the blood vessel in the middle of the image, which is outlined by endothelial cells with typically elongated nuclei (arrowheads). (B) Enlargement of the blood vessel shown in (A). Notice the presence in the lumen of the blood vessel of two cells (arrows) whose nuclear staining pattern suggests that the cells are either multi-nucleated or contain a fragmented single nucleus. In the context of the tissue, these cells most likely represent neutrophilic granulocytes of which a fragmented nucleus is characteristic. (C) The same area of the section, now visualized by TEM, confirming that the two cells in the lumen of the blood vessel represent neutrophils. The upper neutrophil, which is much less electron dense than the lower one, was probably defunct prior to tissue preservation. Note the presence in the blood vessel of two erythrocytes, which were not detected by acridine orange. Scale bars: 20 µm in (A), 10 µm in (B), and 5 µm in (C).

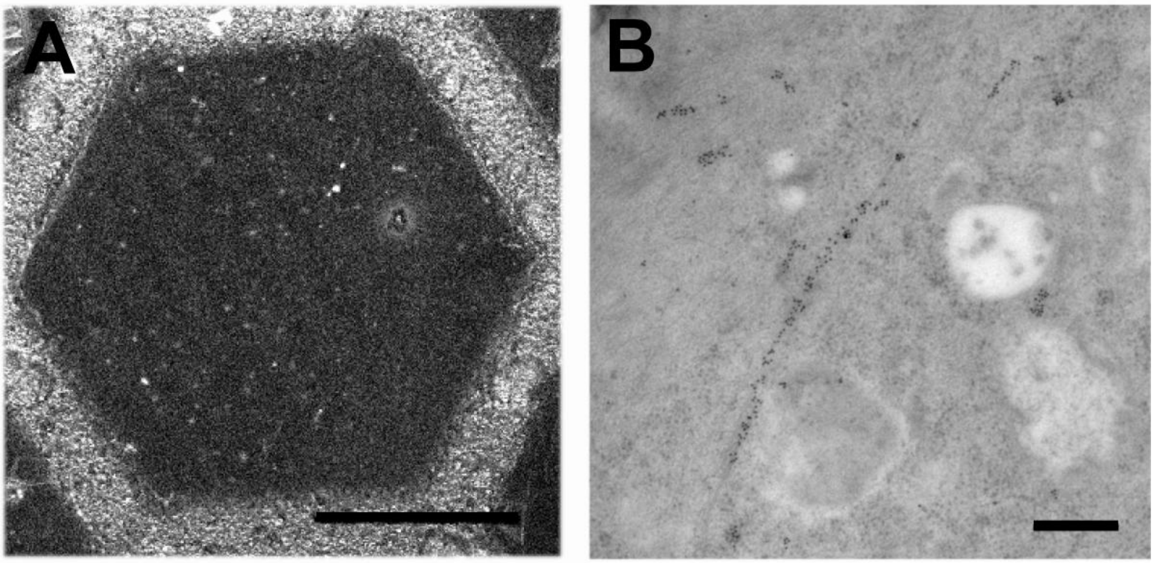

Figure 4: Post-embedding immunolabeling of mouse fibroblast (3T3) cells by monoclonal anti-β-tubulin antibodies, visualized by Alexa Fluor 488 conjugated protein A (panel A) or 15 nm gold protein A (panel B). (A) Fluorescence micrograph of an 80 nm section. Note the absence of a specific fluorescent signal. The bright speckles are nonspecific fluorescent aggregates. (B) Electron micrograph of a subsequent 80 nm section showing, as a positive control, specific immunogold labeling of microtubules in the cortex of a cell. Scale bars: 100 µm in A, 0.5 µm in B.

Appreciable fluorescent signals were obtained with the nuclear stains, SYTOX green (Fig. 5) and DAPI (not shown), and the lectin, wheat-germ agglutinin (WGA) conjugated to Alexa Fluor 488 (Fig. 6). Sections labeled on grid with SYTOX green displayed bright fluorescent nuclei in all tissue layers of rat duodenum. The inner circular and outer longitudinal smooth muscle layers surrounding the submucosa and mucosa were easily distinguished (Fig. 5A, B), as were the crypts of Lieberkühn and villi (Fig. 5C). SYTOX green also labeled the mucous granule field of goblet cells in the intestinal epithelium. Because the mucous granule field is devoid of nucleic acids, it appears that the SYTOX green bound nonspecifically to another component, most likely a mucoid substance, and that this interaction resulted in a fluorescence enhancement comparable to what occurs upon nucleic acid binding.

Lectins have high affinity for glycoconjugates, and are therefore employed as fluorescent probes for the localization of glycoproteins (Roth, 1980). WGA binds selectively to N-acetylglucosamine and N-acetylneuraminic acid residues (Peters et al., 1979). In intestinal tissue, WGA labels among others the mucous granule field and Golgi area of goblet cells (Valentijn et al., 2007). Labeling of ultrathin and thin sections with Alexa Fluor 488 WGA yielded an identical localization pattern (Fig. 6A). Although goblet cells are abundant and therefore easily located by TEM, we found the WGA label very useful to locate sagittally cut goblet cells in which orientation the typical V-shaped architecture of the Golgi apparatus is most informative (Fig. 6B-D). This, as we experienced in a previous study, is a very time consuming exercise when the search for sagittally cut goblet cells is performed by TEM without the help of fluorescence microscopy (Valentijn et al., 2007). In order to find a properly oriented goblet cell, we surveyed approximately 10 TEM grids containing 3 sections each. While previously this took several days by TEM, it now was a matter of hours.

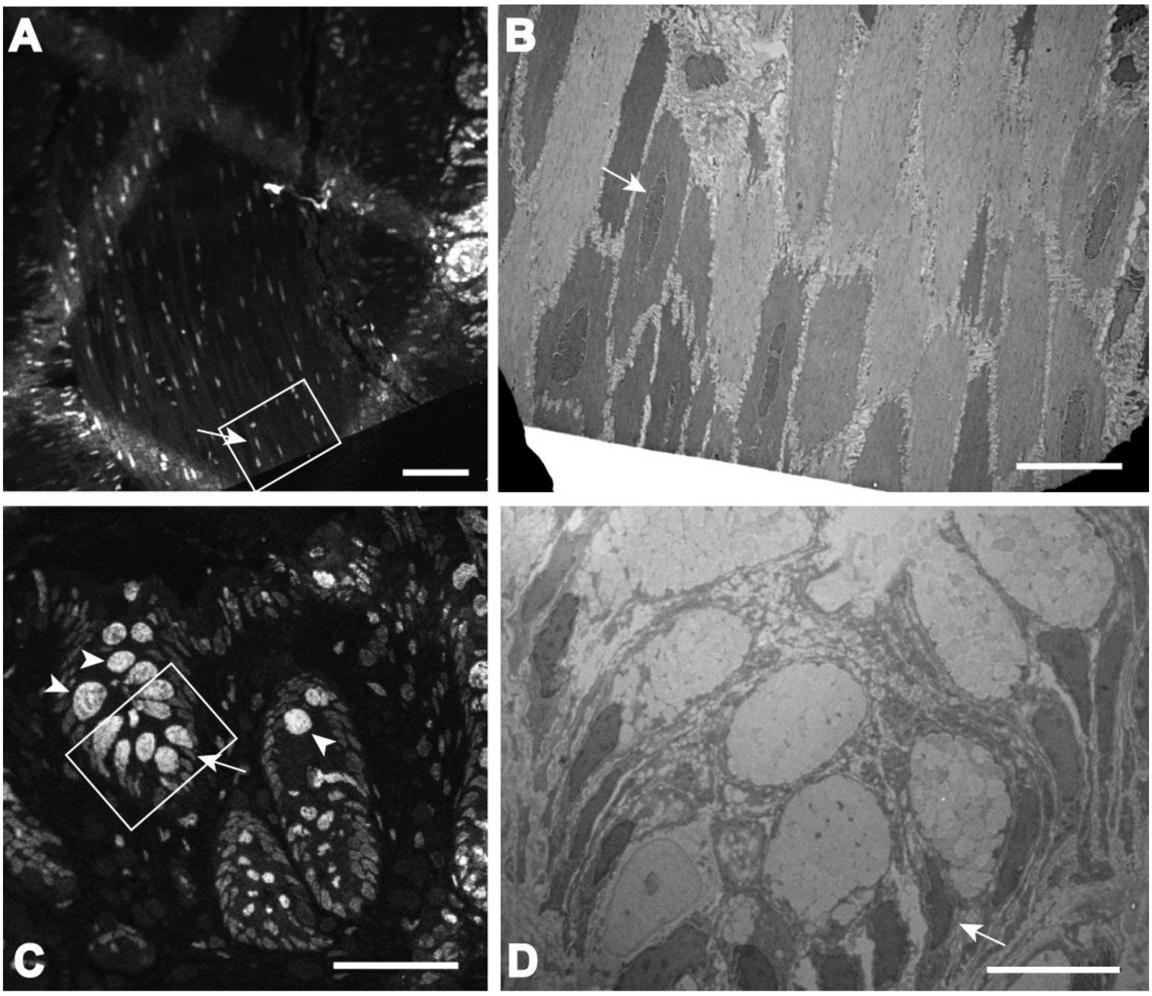

Figure 5: Post-embedding labeling of rat duodenum tissue with SYTOX green, on an 80-nm HM20 section. (A) Fluorescence micrograph giving an overview of the tissue layers present in the section. From left to right, one can distinguish the outer longitudinal smooth muscle layer, the inner circular smooth muscle layer, the connective tissue of the submucosa, the muscularis mucosae, and the mucosa showing the bases of crypts of Lieberkühn. (B) Electron micrograph of the boxed area in (A) showing smooth muscle cells of the inner circular layer. The cells have somewhat shrunken during the PLT procedure. Notice the accurate correlation between the position of the nuclei and the SYTOX green staining pattern in (A). The arrows in (A) and (B) point towards the same nucleus. (C) Fluorescence micrograph of an area in the mucosa showing staining of nuclei principally in the epithelial layer of obliquely cut crypts of Lieberkühn. The mucous granules of the goblet cells are also labeled (arrowheads). (D) Electron micrograph corresponding to the boxed area in (C). The arrow in (C) points towards the same nucleus as the arrow in (D). Scale bars: 50 μm in (A), 10 μm in (B), 50 μm in (C), and 10 μm in (D).

Over the course of the experiments described so far, we made two observations that are potentially of interest to researchers wishing to adopt our approaches. Firstly, the fluorescence is rapidly quenched following electron beam exposure. Therefore, CLEM is a one-way procedure starting with fluorescence microscopy and ending with TEM/electron tomography. Hence it is advisable to scan the whole grid by fluorescence microscopy and document all areas of interest at higher magnification prior to TEM. Secondly, the copper grid bars showed variable degrees of fluorescence. Part of this appeared to be due to autofluorescence, a good example of which can be seen in Fig. 1. Another part, as shown for instance in Figs. 5A and 6A, appeared to result from reflectance of fluorescence (either specific or background) thereby amplifying the overall intensity of the fluorescent signals. However, we cannot exclude that other factors also contributed to the signal amplification over the grid bars, such as metal-enhanced fluorescence (Aslan et al., 2005a; Aslan et al., 2005b).

In general, post-embedding labeling techniques for TEM are incompatible with the fixative and contrasting agent, osmium tetroxide, and the CLEM procedures described herein are no exception. Consequently, TEM micrographs may suffer from lack of contrast, in particular of lipid bilayers for which osmium tetroxide has high affinity. This is obvious, for instance, in the close-up view of the goblet cell Golgi area shown in Fig. 6E, despite the use of uranyl acetate, which also enhances contrast but not of membranes. To overcome this limitation, we explored the potential of using electron tomography as a tool for the generation of 2D images with higher contrast than conventional TEM. The gain in image detail is illustrated in Fig. 6F, which represents a reconstructed image stack of a dual-axis tomogram from the same area as depicted in Fig. 6E. The definition of the Golgi area and immature mucous granules was improved considerably, and ribosomes stood out much better. We next examined the possibility of using less tilt angles for the electron tomography, thereby reducing the time needed for image acquisition at the cost of less 3D resolution. To evaluate the applicability of this approach, we compared 2D reconstructions (defined as the average of a number of digital slices of the tomogram in the plane of the reconstruction) of the same area, using a gradually decreasing number of images taken at regularly spaced tilt angles between +70° and -70°. Analysis of these 2D reconstructions revealed that for the type of specimens we imaged, a minimum number of 31 tilt angles still produced 2D reconstructions in which sufficiently fine 2D detail was preserved (Fig. 7).

Due to the tilting geometry, electron tomograms have anisotropic resolution. As mentioned above, our goal is to generate a 2D image showing ultrastructural detail in the plane of the specimen. To obtain an estimate on the number of images we would require for a given resolution, we can use the relation $d=\pi D/N$ where N is the number of projections with a regular tilt interval ranging from +90° to -90°, D the diameter of a (spherical) object, and d the resolution (Crowther et al., 1970). If we assume a cylindrical object with a diameter (D) of 100 nm, it follows from the above equation that for a tilt increment of 1°, yielding 181 projections, the resolution is 1.6 nm; for a tilt increment of 2°, yielding 91 projections, the resolution is 3.5 nm; for a tilt increment of 4°, yielding 46

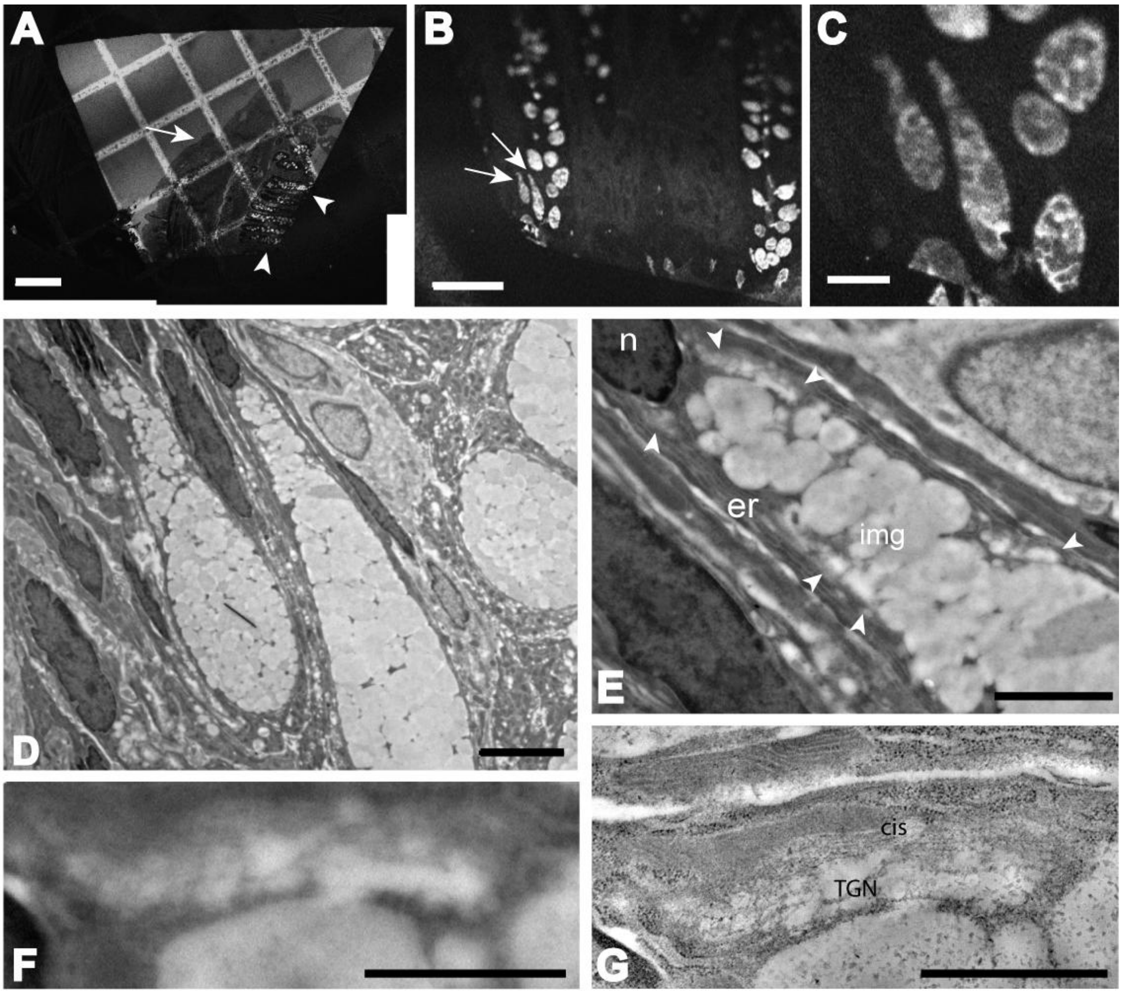

Figure 6: Correlative light an electron tomography of a sagittally cut goblet cell. An HM20-embedded rat duodenum section was labeled on a TEM-grid with Alexa Fluor 488-conjugated WGA. (A) Overview of the whole section imaged by fluorescence microscopy. The image was generated by combining (stitching) of 5 slightly overlapping fluorescence micrographs. Background fluorescence of the HM20 exposes the boundaries of the embedded tissue (arrow). Parallel dotted lines of fluorescence (arrowheads) denote crypts of Lieberkühn. (B) Higher magnification image showing fluorescent labeling by WGA of the mucous granule field of goblet cells in crypts of Lieberkühn. Many mucous granule fields are circular or oval-shaped, indicating that the Golgi apparatus of these goblet cells is located in a plane outside of the section. In two goblet cells (arrows), the fluorescence of the mucous granule field blends into the V-shaped Golgi area that is also labeled by WGA, indicating that these cells were sagitally cut, and indicating further that these cells are suitable for ultrastructural analysis of the Golgi area. (C) Zoom of the two goblet cells denoted in (B). (D) Electron micrograph of the same area shown in (C), confirming that the two goblet cells denoted in (B) were sectioned sagitally. (E) Enlargement of the Golgi area in the right-hand goblet cell shown in (D). The Golgi area (arrowheads) starts above the nucleus (n) and surrounds an area of immature mucous granules (img). The Golgi area itself is surrounded by a prominent endoplasmatic reticulum (er). (F) Higher magnification electron micrograph of a Golgi stack corresponding to the boxed area in (E). Because the tissue could not be contrasted with osmium tetroxide, due to incompatibility with fluorescent probes, the micrograph lacks contrast and definition. (G) 2D representation of the same Golgi area shown in (F), generated by averaging a stack of 10 digital slices of a tomographic reconstruction. The densely packed early Golgi cisternae (cis) and the dilated trans-Golgi network (TGN) are now easily recognized. Note also the dramatic improvement of detail in the endoplasmic reticulum, where individual ribosomes are now easily discerned. Scale bars: 300 µm in (A), 50 µm in (B), 10 µm in (C), 5 µm in (D), 2 µm in (E), 1 µm in (F), 1 µm in (G).

projections, the resolution is 6.8 nm. In practice, projections can be obtained only from tilt angles between +70° and -70°, and as a result there is a missing wedge of information so that the actual resolution will be lower (McIntosh et al., 2005). For many applications of electron tomography on resin-embedded structures a pixel size in the order of 1 nm would be suitable to explore the structures of interest. Thus by averaging 10 successive digital slices in the plane of the specimen (z-axis), each 1 nm thick, a 2D xy-plane is generated that corresponds to a section thickness of around 10 nm, which is in the order of magnitude of the theoretical z-resolution (especially when an elongation factor is taken into account as a result of the missing wedge). In our observations and for our type of specimen, we found that averaging of approximately 10 slices provided 2D images with sufficiently high contrast and detail; when more than 15 slices were averaged, the images appeared more blurred as a result of the superimposed structures along the z-axis in combination with the lack of resolution in the z-direction (due to the relatively low resolution angular sampling).

The contrast enhancement that accompanies the electron tomography approach should provide sufficient ultrastructural detail for many questions in cell biology and pathology that require CLEM. If higher resolution information is required, the use of scanning transmission electron microscopy (STEM) can be considered. Thus Carlemalm and Kellenberger (1982) have shown that imaging of unstained resin-embedded tissue by STEM in Z-contrast mode can reveal protein complexes that are not visible in other imaging modes using a heavy metal stain for contrast.

Figure 7: Contrast enhancement in 2D representations of non-osmicated duodenal tissue using a simplified tomography procedure. Minimum requirements on angular tilt increments for the generation of 2D representations of averaged electron tomography data. (A) Conventional transmission electron micrograph of an area in a goblet cell (rat duodenum) containing endoplasmic reticulum. The black dots represent 15-nm colloidal gold particles used as fiducial markers for the alignment of projection images for tomographic reconstruction. (B) through (E) Tomograms of the same area as shown in (A), reconstructed using 126 projections of 1° increments between tilt angles of +65° and -60° (B), 63 projections with 2° increments (C), 31 projections with 4° increments (D), or 16 projections with 8° increments (E). Each image represents an averaged stack of 10 digital slices, corresponding to an 8-nm thick section. The image detail in the reconstructions based on 126, 63, and 31 projections is much improved in comparison to (A), as evidenced for instance by the definition of the ribosomes. With only 16 projections, the image is deteriorated and displays artifactual striping at the positions of the high-contrast fiducial markers. (F) Same reconstruction as in (D) but now the image is based on the average of 25 consecutive digital slices, corresponding to a 14-nm thick section. Note that the image becomes blurred due to the increased stack size. Scale bar: 0.5 µm in all images.

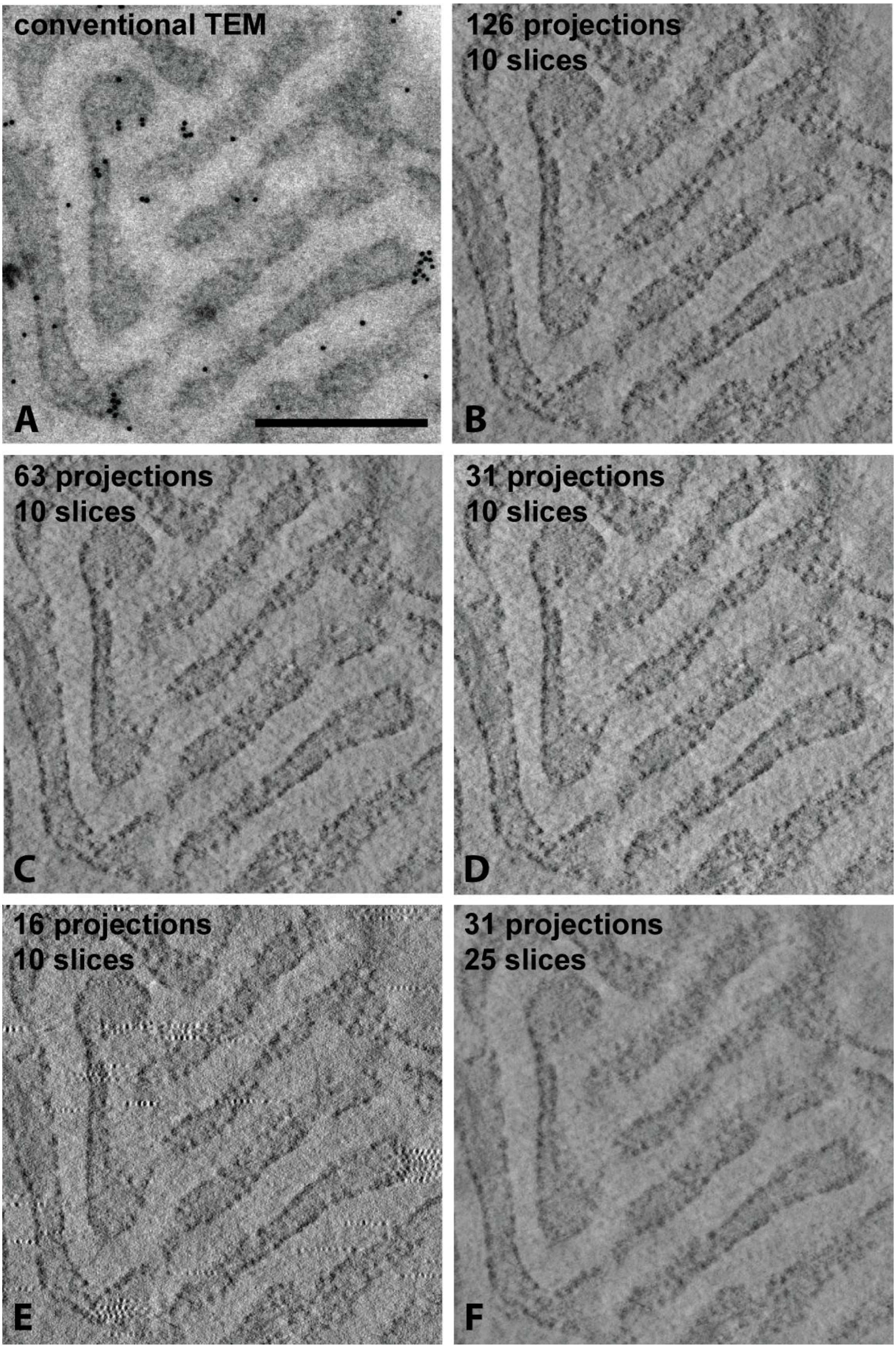

conventional TEM
A
126 projections
10 slices
B
63 projections
10 slices
C
31 projections
10 slices
D
16 projections
10 slices
E
31 projections
25 slices
F

Concluding Remarks

We have shown that CLEM can be performed directly on ultrathin and thin plastic sections using straightforward, generally applicable specimen preparation approaches. We exemplified the use of CLEM with several types of fluorescent stains and probes. The nucleic acid stains, acridine orange, SYTOX green, and DAPI, allow for the identification of dividing cells and cells with characteristic nuclei or nucleoli, while providing clues for orientation in complex tissues. And the lectin, WGA, highlights glycoprotein-rich cells and organelles such as goblet cells, mucous granules, and the Golgi apparatus. Using the TEM grid bars and the position of the sections as a visual coordinate system, areas of interest that are mapped by fluorescence microscopy are readily retrieved by TEM. The fluorescent dyes are incompatible with osmium tetroxide, but the resulting decrease in TEM contrast can be counterbalanced by the increase in contrast that is associated with electron tomography. If the desired endpoint of the CLEM procedure is a 2D electron micrograph of an area of interest, we propose a streamlined electron tomography procedure using a minimum amount of tilt images to produce a 2D image with high resolution and improved contrast as a result of averaging 2D slices of the tomogram in the z-direction.

Acknowledgements

The authors wish to thank Karen A. Jansen for the tomography, and Jos Onderwater and Ronald Limpens for expert technical assistance. Human tissue samples were kindly provided by Dr. Jan Lindeman, M.D. (Department of Pathology, Leiden University Medical Center). We also thank prof. Willem van Ewijk for helpful discussions.

References

Amsterdam, A., T.E. Solomon, and J.D. Jamieson, 1978. Sequential dissociation of the exocrine pancreas into lobules, acini, and individual cells. Methods Cell Biol 20: 361-78.

Aslan, K., R. Badugu, J.R. Lakowicz, and C.D. Geddes, 2005a. Metal-enhanced fluorescence from plastic substrates. J Fluoresc 15: 99-104.

Aslan, K., I. Gryczynski, J. Malicka, E. Matveeva, J.R. Lakowicz, and C.D. Geddes, 2005b. Metal-enhanced fluorescence: an emerging tool in biotechnology. Curr Opin Biotechnol 16: 55-62.

Biel, S.S., K. Kawaschinski, K.P. Wittern, U. Hintze, and R. Wepf, 2003. From tissue to cellular ultrastructure: closing the gap between micro- and nanostructural imaging. J Microsc 212: 91-9.

Braet, F., E. Wisse, P. Bomans, P. Frederik, W. Geerts, A. Koster, L. Soon, and S. Ringer, 2007. Contribution of high-resolution correlative imaging techniques in the study of the liver sieve in three-dimensions. Microsc Res Tech.

Cai, Z., J. Manavis, K. Cash, P.D. Thompson, and P.C. Blumbergs, 2005. Immunohistochemical staining of epoxy resin sections of peripheral nerve. Appl Immunohistochem Mol Morphol 13: 292-4.

Carlemalm, E., and E. Kellenberger, 1982. The reproducible observation of unstained embedded cellular material in thin sections: visualisation of an integral membrane protein by a new mode of imaging for STEM. EMBO J. 1:63-67

Corstjens, P.L., S. Li, M. Zuiderwijk, K. Kardos, W.R. Abrams, R.S. Niedbala, and H.J. Tanke, 2005. Infrared up-converting phosphors for bioassays. IEE Proc Nanobiotechnol 152: 64-72.

Crowther, R.A., D.J. DeRosier, and A. Klug, 1970. The reconstruction of a three-dimensional structure from projections and its application to electron microscopy. Proc. Roy. Soc. Lond. A. 317: 319-340.

Deerinck, T.J., B.N. Giepmans, B.L. Smarr, M.E. Martone, and M.H. Ellisman, 2007. Light and electron microscopic localization of multiple proteins using quantum dots. Methods Mol Biol 374: 43-54.

Giepmans, B.N., S.R. Adams, M.H. Ellisman, and R.Y. Tsien, 2006. The fluorescent toolbox for assessing protein location and function. Science 312: 217-24.

Giepmans, B.N., T.J. Deerinck, B.L. Smarr, Y.Z. Jones, and M.H. Ellisman, 2005. Correlated light and electron microscopic imaging of multiple endogenous proteins using Quantum dots. Nat Methods 2: 743-9.

Grabenbauer, M., W.J. Geerts, J. Fernadez-Rodriguez, A. Hoenger, A.J. Koster, and T. Nilsson, 2005. Correlative microscopy and electron tomography of GFP through photooxidation. Nat Methods 2: 857-62.

Groos, S., E. Reale, and L. Luciano, 2001. Re-evaluation of epoxy resin sections for light and electron microscopic immunostaining. J Histochem Cytochem 49: 397-406.

Jones, S., S.K. Chapman, P.R. Crocker, G. Carson, and D.A. Levison, 1982. Combined light and electron microscope in routine histopathology. J Clin Pathol 35: 425-9.

Koster, A.J., and J. Klumperman, 2003. Electron microscopy in cell biology: integrating structure and function. Nat Rev Mol Cell Biol Suppl: SS6-10.

Kremer, J.R., D.N. Mastronarde, and J.R. McIntosh, 1996. Computer visualization of three-dimensional image data using IMOD. J Struct Biol 116: 71-6.

Lentz, T.L., 1971. Cell Fine Structure W. B. Saunders Company, Philadelphia.

McIntosh, R., D. Nicastro, and D. Mastronarde, 2005. New views of cells in 3D: an introduction to electron tomography. Trends Cell Biol 15: 43-51.

McNary, W.F., Jr., R.C. Rosan, and J.A. Kerrigan, 1964. Fluorescent Microscopy of Thin Sections as an Adjunct to Electron Microscopy. J Histochem Cytochem 12: 216-7.

Mironov, A.A., R.S. Polishchuk, and A. Luini, 2000. Visualizing membrane traffic in vivo by combined video fluorescence and 3D electron microscopy. Trends Cell Biol 10: 349-53.

Mori, M., G. Ishikawa, T. Takeshita, T. Goto, J.M. Robinson, and T. Takizawa, 2006. Ultrahigh-resolution immunofluorescence microscopy using ultrathin cryosections: subcellular distribution of caveolin-1alpha and CD31 in human placental endothelial cells. J Electron Microsc (Tokyo) 55: 107-12.

Najlah, M., and A. D'Emanuele, 2006. Crossing cellular barriers using dendrimer nanotechnologies. Curr Opin Pharmacol 6: 522-7.

Peters, B.P., S. Ebisu, I.J. Goldstein, and M. Flashner, 1979. Interaction of wheat germ agglutinin with sialic acid. Biochemistry 18: 5505-11.

Pfeiffer, S., M. Beese, M. Boettcher, K. Kawaschinski, and K. Krupinska, 2003. Combined use of confocal laser scanning microscopy and transmission electron microscopy for visualisation of identical cells processed by cryotechniques. Protoplasma 222: 129-37.

Powell, R.D., C.M. Halsey, and J.F. Hainfeld, 1998. Combined fluorescent and gold immunoprobes: reagents and methods for correlative light and electron microscopy. Microsc Res Tech 42: 2-12.

Rigler, R., Jr., 1966. Microfluorometric characterization of intracellular nucleic acids and nucleoproteins by acridine orange. Acta Physiol Scand Suppl 267: 1-122.

Robertson, D., P. Monaghan, C. Clarke, and A.J. Atherton, 1992. An appraisal of low-temperature embedding by progressive lowering of temperature into Lowicryl HM20 for immunocytochemical studies. J Microsc 168: 85-100.

Roth, J., 1980. The use of lectins as probes for carbohydrates--cytochemical techniques and their application in studies on cell surface dynamics. Acta Histochem Suppl 22: 113-21.

Steven, A.C., and U. Aebi, 2003. The next ice age: cryo-electron tomography of intact cells. Trends Cell Biol 13: 107-10.

Svitkina, T.M., and G.G. Borisy, 1998. Correlative light and electron microscopy of the cytoskeleton of cultured cells. Methods Enzymol 298: 570-92.

Takizawa, T., and J.M. Robinson, 2000. FluoroNanogold is a bifunctional immunoprobe for correlative fluorescence and electron microscopy. J Histochem Cytochem 48: 481-6.

Takizawa, T., and J.M. Robinson, 2003. Ultrathin cryosections: an important tool for immunofluorescence and correlative microscopy. J Histochem Cytochem 51: 707-14.

Tome, F.M., D. Chateau, A. Helbling-Leclerc, and M. Fardeau, 1997. Morphological changes in muscle fibers in oculopharyngeal muscular dystrophy. Neuromuscul Disord 7 Suppl 1: S63-9.

Valentijn, J.A., L. van Weeren, A. Ultee, and A.J. Koster, 2007. Novel localization of Rab3D in rat intestinal goblet cells and Brunner's gland acinar cells suggests a role in early Golgi trafficking. American Journal of Physiology: Gastrointestinal and Liver Physiology 293: G165-77.

Valentijn, K.M., F.D. Gumkowski, and J.D. Jamieson, 1999. The subapical actin cytoskeleton regulates secretion and membrane retrieval in pancreatic acinar cells. J Cell Sci 112 (Pt 1): 81-96.